Nuclear Science and Techniques (2025) 36:85
https://doi.org/10.1007/s41365-025-01647-x

Zero-valent silver nanoparticles functionalized populus tomentosa fiber for efficient capture and immobilization of iodine vapor

Yu Fang[1,2] · Hui Zhu[1,2] · Pei Chen[1,2] · Fang Liu[3] · Yong Yi[4] · Jian Zhou[5] · Tao Duan[5,6] · Jie-Hong Lei[1,2]

Received: 15 January 2024 / Revised: 15 May 2024 / Accepted: 16 May 2024 / Published online: 20 March 2025

Abstract

With the rapid development of nuclear energy, the removal of radioactive iodine generated during spent fuel reprocessing has become increasingly important. Based on the unique straw-like structure of populus tomentosa fiber (PTF) and the highly active iodine vapor capture ability of zero-valent silver nanoparticles (PTF@Ag^0NP), an Ag^0NP composite functional material with highly efficient iodine vapor capture capability was synthesized from biowaste PTF through ultrasonic and high-temperature hydrothermal methods in this study. The iodine capture experiment demonstrated that PTF@Ag^0NP exhibits rapid iodine capture efficiency, reaching dynamic equilibrium within 4 h and a maximum capture capacity of 1008.1 mg/g. Density functional theory calculations show that PTF@Ag^0NP exhibits extremely high chemical reactivity toward iodine, with a reaction binding energy of −2.88 eV. Additionally, the molecular dynamics of PTF@Ag^0NP indicate that there is no atomic displacement at 77 °C, indicating the excellent temperature stability of the material at the operating temperature. The capture mechanism suggests that iodine vapor primarily reacts with Ag^0NP to form AgI, and that the hydroxyl groups in PTF can also effectively capture iodine vapor by adsorption induction. In conclusion, PTF@Ag^0NP is expected to be an effective candidate adsorbent material for removing radioactive iodine vapor from exhaust gases during spent fuel reprocessing.

Keywords Ag^0NP · Populus tomentosa fiber · Iodine vapor · Capture and immobilization · DFT calculations

1 Introduction

With the rapid development of nuclear energy, the attention of researchers to the reprocessing of spent radioactive fuel has also increased [1]. It is projected that by 2030, global electricity production from nuclear reactors will increase from the current 11.3% to over 23% [2, 3]. However, this growth will also result in the significant annual generation of spent radioactive fuel [2]. Safe and economical management

This work was supported by the Sichuan Outstanding Young Scientific and Technological Talents Project (No. 2021JDJQ0016), Doctoral Initiation Project of China West Normal University (No. 22kE043), and Science and Technology Project of Sichuan Province (No.2022NSFSC0388).

✉ Hui Zhu
zhuhui61@cwnu.edu.cn

✉ Jie-Hong Lei
leijiehong@cwnu.edu.cn

[1] Research Center for New Energy Materials, China West Normal University, Nanchong 637002, China

[2] School of Physics and Astronomy, China West Normal University, Nanchong 637002, China

[3] College of Materials and Chemistry & Chemical Engineering, Chengdu University of Technology, Chengdu 610059, China

[4] School of Materials and Chemistry, Southwest University of Science and Technology, Mianyang 621010, China

[5] State Key Laboratory of Environment-friendly Energy Materials, School of National Defense Science & Technology, Southwest University of Science and Technology, Mianyang 621010, China

[6] Tianfu Institute of Research and Innovation, Southwest University of Science and Technology, Chengdu 610299, China

of spent fuel will become a critical factor limiting the development of nuclear energy. The reprocessing of spent fuel generates a large amount of radioactive iodine isotopes, which exhibit strong diffusion capabilities and are prone to be released and spread at high temperatures [3]. These isotopes must be properly captured and immobilized [4]. Owing to the long half-life of ^{129}I (1.52×10^7 years), it continues to radiate and accumulate in the environment and is prone to accumulation in tissues such as the thyroid; this can lead to thyroid dysfunction and even thyroid cancer, posing a serious hazard to human health and the ecological environment [5]. Therefore, it is of great practical significance to effectively capture and immobilize radioactive iodine vapor during spent fuel reprocessing.

Current treatment technologies for radioactive iodine vapor include wet scrubbing and solid capture methods [6]. Wet scrubbing techniques primarily include acid scrubbing, alkaline scrubbing, mercury column scrubbing, and electrolytic scrubbing, which are popular because they allow for the precise adjustment of solution parameters according to demand [6]. However, owing to high operational costs, difficulties in the disposal of liquids after scrubbing, and the possibility of secondary pollution, its practical applications are limited [4]. On the other hand, solid capture technologies exhibit significant advantages over wet scrubbing techniques because of their simplicity of operation, reliability, ease of post-treatment, and lower maintenance and operational costs [4, 7]. Materials used to capture radioactive iodine vapor include activated carbon [8], porous zeolites [9], aerogels [10], metal-organic frameworks (MOFs) [11], and covalent organic frameworks (COFs) [12]. Activated carbon materials have low preparation costs and high iodine capture capacity but are prone to aging and secondary pollution [8]. Porous zeolites have strong resistance to environmental interference and high capture efficiency; therefore, they are currently the mainstream commercial iodine capture materials. However, they are expensive, have a limited capture capacity, and are prone to saturation, requiring frequent replacement and maintenance [13, 14]. Aerogel materials exhibit excellent iodine capture efficiency owing to their nanoporous network structure; however, their complex and cumbersome preparation conditions and low mechanical strength severely limit their practical applications [10]. MOFs and COFs have been a major research hotspot in recent years. They are widely used in ion separation [15, 16], photocatalysis [17], and radionuclide capture [18, 19] and have achieved ground-breaking results [20, 21]; however, their high cost and complex preparation have hindered their large-scale application [22]. Therefore, low-cost, easy-to-prepare, and high-performance iodine capture materials that can be produced on a large scale are currently the focus of research [23].

Due to the strong affinity of silver for iodine, silver-based capture materials exhibit excellent iodine capture selectivity, high capture efficiency, and strong iodine immobilization capacity, making them among the most effective iodine vapor capture materials [24–26]. Currently, Ag is widely used as an active material in zeolites [25], aerogels [10], and MOFs [26]. However, because most of these substrates only exhibit a porous structure, their iodine capture capacity is significantly influenced by the amount of Ag loaded. Therefore, optimizing the interaction between the adsorbent and iodine and pursuing a higher capture efficiency based on ensuring reliable iodine immobilization ability are development directions for silver-based capture agents. Owing to the nanoscale size effect, nanoscale zero-valent silver possesses high chemical activity and iodine capture selectivity, making it an ideal active material for capturing iodine vapor. However, Ag exhibits spontaneous aggregation, making obtaining effective nanoscale particles difficult. Therefore, the suppression of the spontaneous aggregation of nanosilver is one of the current challenges for silver-based materials [27]. Duan et al. successfully enhanced the iodine capture performance of a material by loading numerous nanoscale zero-valent silver particles onto an activated collagen fiber (ACF) through the construction of highly dispersed multilayer active interfaces with bayberry tannin [27]. Capron et al. found that hydroxyl-rich cellulose can interact ionically with silver ions in a silver nitrate solution at room temperature and can be used to reduce and prepare composite materials in situ with loaded nanoscale zero-valent silver particles using hydrogen peroxide [28]. Gong et al. further demonstrated that cellulose can yield nanoscale zero-valent silver particles of different sizes when reacted with a silver nitrate solution at different hydrothermal temperatures [29]. These studies show that nanosilver has a specific recognition effect on iodine and provides a new way to solve the aggregation problem of nanosilver.

In this study, by taking advantage of the hollow microtubule structure and hydroxyl-rich properties of the populus tomentosa fiber (PTF), combined with the strong complexation ability of cellulose hydroxyl to silver ions, we successfully complexed silver ions on both the inner and outer surfaces of PTF microtubules using ultrasonication and a hydrothermal method in an innovative way. By utilizing the strong reducing action of $NaBH_4$ at the hydroxyl passivation sites, nano zero-valent silver particles were successfully reduced. The spatial hindrance effect of the hydroxyl passivation sites effectively solves the problem of nanosilver particle aggregation. Utilizing the highly specific binding ability of zero-valent silver nanoparticles to iodine, the efficient capture and immobilization of iodine vapor can be achieved. This material has the advantages of a simple preparation process, low cost, stable properties, large-scale production capability, and high iodine vapor capture capacity, making it a promising candidate for the efficient removal of radioactive iodine from exhaust gases during spent fuel reprocessing.

2 Materials and methods

2.1 Materials

The PTF was purchased from Suqian Landscaping and Greening Engineering Co., Ltd. Silver nitrate ($AgNO_3$, AR), sodium borohydride ($NaBH_4$, AR), iodine (I_2, AR), and anhydrous ethanol (C_2H_5OH, AR) were all purchased from Shanghai Macklin Biochemical Technology Co., Ltd. The reagents used in this experiment were used directly without further purification.

2.2 Preparation of PTF@Ag^0NP

The preparation of the nanoscale zero-valent silver-functionalized Populus tomentosa fiber straw-like hydrothermal carbon material (PTF@Ag^0NP) was based on the following steps with subsequent improvements [30]. A certain mass of $AgNO_3$ was dissolved in 30 mL of deionized water, followed by the addition of 0.1 g PTF. The mixture was stirred for 2 h and subjected to ultrasonic complexation for 48 h. The resulting mixture was transferred to a 50 mL Teflon-lined hydrothermal reaction vessel and subjected to hydrothermal treatment at 160 °C for 2 h. After filtration and washing, a straw-like hydrothermal carbon material with Ag^+-complexed PTF was obtained. The hydrothermal carbon material was then reduced using a 0.3 mol/L $NaBH_4$ aqueous solution at room temperature for 8 h. After filtration and repeated washing, it was dried in a vacuum drying oven at 75 °C for 24 h to obtain PTF@Ag^0NP.

2.3 Characterization

An FTIR spectrometer (FTIR, PE, Spectrum Two N, USA) was used to record the Fourier transform infrared spectrum information (FTIR) of the material using the KBr tableting method in the range of 400 ~ 4000 cm^{-1}. A fully automatic specific surface area porosity analyzer (ASAP2460) was used to determine the nitrogen adsorption and desorption curve (BET) of the material. A thermogravimetric analyzer (NETZSCH TG 209F3) was used to analyze the thermogravimetric loss of the material under a nitrogen atmosphere at a heating rate of 10 °C/min to 500 °C. An XRD diffractometer (TD-3500, Dandong Tongda Technology Co., Ltd) was used to measure the X-ray diffraction pattern characteristics of the material in the range of $2\theta = 5° \sim 80°$. Field-emission scanning electron microscopy (FE-SEM, 200 kV, Ultra55, Carl-Zeiss, Germany) was used to determine the micromorphological characteristics of the materials. X-ray spectroscopy (EDX, Ultra 55, Carl-Zeiss) was used to observe the elemental distribution characteristics of the material surface. The material X-ray photoelectron spectroscopy characteristics (XPS) were recorded using an Escalab250 spectrometer (Thermo, Fisher Corporation, USA). A UV spectrophotometer (UV-3150) was used to record the UV-visible light absorption spectral characteristics of the material solution.

2.4 Iodine vapor capture experiment

In this study, nonradioactive crystalline iodine was used to replace radioactive iodine in the experiments. Initially, 0.5 g of crystalline iodine was placed in a 500 mL wide-mouth bottle, whereas 20 mg of PTF@Ag^0NP was loaded into a 5 mL crucible. The crucible was then placed in a wide-mouth bottle, capped, and placed in an oven at 75 °C for iodine vapor capture. At different time intervals, the wide-mouthed bottle was removed from the oven and placed in a desiccator to cool to room temperature. Subsequently, the capture of iodine vapor by the PTF@Ag^0NP was determined using the gravimetric method [27]. The calculation is shown in Eq. (1):

$$Q = (m_2 - m_1)/m_1 \times 1000, \tag{1}$$

where Q (mg/g) is the amount of iodine captured and m_1 (mg) and m_2 (mg) represent the initial and final weights of the material following iodine capture, respectively. The average value for each material was obtained from three parallel experiments.

2.5 Iodine desorbed experiment

5.0 mg of the captured iodine material was weighed multiple times and, respectively, placed them in a 5 mL absolute ethanol solution. At different time intervals, selected one of the aforementioned solutions and extracted 1 mL, which was then diluted tenfold with absolute ethanol. The spectral characteristics of the diluted solution were determined from 240 nm to 600 nm by UV-Vis spectrophotometer to determine the concentration of iodine in the solution (absorption peak intensity at 291 nm and 360 nm) [7].

2.6 Kinetics of iodine capture

The iodine vapor capture curves of PTF@Ag^0NP were fitted using the pseudo-first-order kinetic equation (Eq. 2) and pseudo-second-order kinetic equation (Eq. 3):

$$Q_t = Q_e(1 - e^{-k_1 t}), \tag{2}$$

$$Q_t = k_2 t Q_e^2/(1 + k_2 Q_e t), \tag{3}$$

where Q_t (mg/g) and Q_e (mg/g) are the iodine adsorption capacities of PTF@Ag^0NP at certain and equilibrium times, respectively. k_1 (h^{-1}) and k_2 ($g \cdot mg^{-1} \cdot h^{-1}$) are the rate constants of the pseudo-first- and pseudo-second-order kinetic equations, respectively. where t (h) is the contact time [31].

2.7 DFT calculations

All density functional theory calculations were performed using the Dmol3 module, as implemented in the Materials Studio software [32]. The Perdew-Burke-Ernzerhof (PBE) generalized gradient approximation (GGA) was used as the exchange-correlation interaction functional [33]. Dispersion correction per Grimme (DFT-D2) was employed to treat weak van der Waals (vdW) interactions [34]. The convergence tolerance values for the energy, maximum force, and maximum displacement were set as 1.0×10^{-6} Ha, 0.001 Ha/Å, and 0.002 Å, respectively. To avoid the interactions imposed by the introduction of periodic boundary conditions, a vacuum space of 40 Å was adopted, which was confirmed to be sufficiently large to attenuate factitious interactions. Brillouin zone was sampled using a k-point of 2×2×1, and the global orbital cutoff was set to 4.5 Å to obtain high-quality results. To evaluate the thermal stability of PTF@Ag^0NP, ab initio molecular dynamic (AIMD) simulations were performed at 77 °C within the NVT ensemble for 5 ps. To estimate the stability of the Ag adsorbed on PTF surface, the binding energy (E_b) was calculated as shown in Eq. (4):

$$E_b = E_{PTF@Ag^0NP} - E_{PTF} - E_{Ag}, \quad (4)$$

where $E_{PTF@Ag^0NP}$ represents the energy of PTF@Ag^0NP, E_{PTF} represents the energy of PTF, and E_{Ag} represents the energy of silver. Similarly, to evaluate the iodine capture capability of PTF@Ag^0NP, the calculation method for adsorption energy (E_{abs}) is shown in Eq. (5):

$$E_{abs} = E_{PTF@Ag^0NP\text{-}I} - E_{PTF@Ag^0NP} - E_{iodine}, \quad (5)$$

where $E_{PTF@Ag^0NP\text{-}I}$ denotes the energy of PTF@Ag^0NP-I, $E_{PTF@Ag0NP}$ denotes the energy of PTF@Ag^0NP, and E_{iodine} denotes the energy of the iodine molecules.

3 Results and discussion

3.1 Preparation of PTF@Ag^0NP

PTF is a biomass material primarily composed of cellulose, hemicellulose, and a small amount of lignin and lipids. It has a unique straw-like hollow microtubule structure with a hollowing rate as high as 90 % [35]. After modification, the surface and inner surface of the PTF can release numerous hydroxyls and other active sites, making it a good substrate for capturing materials [36]. The preparation process for PTF@Ag^0NP is illustrated in Fig. 1. First, the PTF was immersed in a silver nitrate solution to obtain a precursor mixture. The mixture was then subjected to ultrasonication and a high-temperature hydrothermal treatment. Owing to their strong electron affinity, silver ions readily form stable complexes with the lone pair of electrons on the hydroxyl groups through coordination bonds under the influence of ultrasonic and hydrothermal conditions. This ultimately

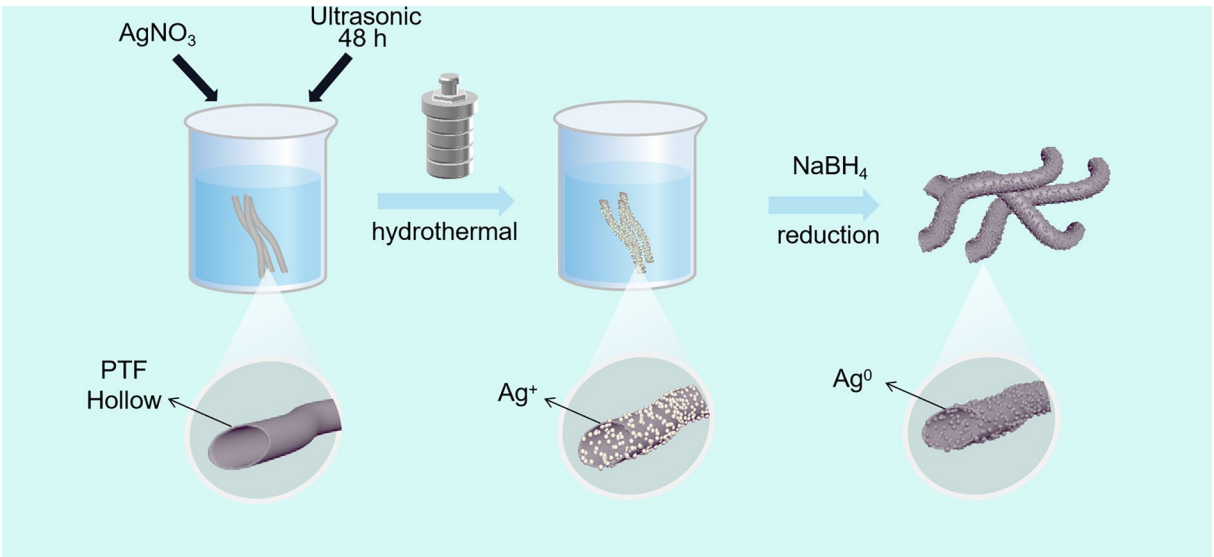

Fig. 1 (Color online) Schematic diagram of the preparation process for PTF@Ag^0NP

results in the loading of silver ions onto the cellulose fibers, effectively addressing the issue of silver nanoparticle aggregation [28, 37]. Finally, a strong reducing agent, $NaBH_4$, was used to further reduce Ag^+ to Ag^0, thus enhancing its reactivity toward iodine vapor. At this stage, the hydroxyl groups also provided stable passivation sites for the nanoscale zero-valent Ag particles, preventing their detachment from the PTF [38]. To investigate the influence of varying concentrations of Ag^+ on the complexation capacity of the PTF, silver nitrate solutions with concentrations of 0.2 g/L, 0.5 g/L, and 2.0 g/L were prepared. Subsequently, we synthesized three distinct types of PTF@Ag^0NP materials with varying Ag content. As shown in Table S1, ICP-OES was used to determine the silver content in the materials, and the amount of silver was shown to gradually increase with increasing silver nitrate concentrations. To further verify the effect of different silver contents on the iodine capture performance of the materials, the iodine capture capacity of PTF and three different silver contents of the PTF@Ag^0NP materials were determined (Fig. S1). The results showed that after loading the nanosilver particles, the iodine capture capacity of PTF@Ag^0NP was significantly improved compared to PTF. Meanwhile, no significant difference was found in iodine capture between the materials prepared with a silver content of 2.0 g/L and those prepared with 0.5 g/L, which may have been caused by the agglomeration of nanosilver into large particles during the preparation of high concentrations of silver nitrate. To further enhance the utilization efficiency of Ag^+ and effectively generate zero-valent silver nanoparticles, this study conducted a comprehensive characterization and analysis of the material (PTF@Ag^0NP) prepared with a 0.5 g/L silver nitrate solution.

3.2 Characterization

FTIR analysis

To explore the changes in the functional groups throughout the material preparation and iodine capture processes, the FTIR spectra of PTF, PTF@Ag^0NP, and PTF@Ag^0NP-I are shown in Fig. 2a. In the PTF spectrum, the absorption peaks at 3372 cm^{-1} and 2914 cm^{-1} are attributed to the stretching vibrations of -OH and C-H, respectively [7]. The absorption peak at 1740 cm^{-1} is attributed to the stretching vibration characteristic of the carbonyl group, and the peak at 1645 cm^{-1} is attributed to the vibration characteristic of the protein amide [39]. The absorption peak at 1424 cm^{-1} is attributed to the bending vibration characteristic of the hydroxyl group [40], and the peak at 1038 cm^{-1} is attributed to the stretching vibration characteristic of the C-O bond [36, 41]. This infrared spectrum exhibits the typical structural features of cellulose [42]. Compared with PTF, the characteristic absorption peaks at 1740 cm^{-1} and 1645 cm^{-1} in PTF@Ag^0NP disappear, suggesting that lipids and protein-like substances may have been removed from PTF during the high-temperature hydrothermal processes [43]. The characteristic peak of the hydroxyl group bending vibration shifts from 1424 cm^{-1} to 1411 cm^{-1}, possibly owing to the electron transfer caused by the complexation of Ag^+ with the hydroxyl groups, resulting in changes in the hydroxyl group stretching vibration. After iodine vapor capture, the characteristic hydroxyl vibration peak at 1411 cm^{-1} in PTF@Ag^0NP-I infrared spectrum is enhanced, possibly because more hydroxyl sites are released after the reaction with silver.

BET analysis

Nitrogen adsorption–desorption experiments were conducted to investigate the changes in the specific surface area throughout the material preparation and iodine capture processes. The results are presented in Fig. 2b. PTF not only has a hollow microtubule structure but also has a large surface area, with the specific surface area of 4.716 m^2/g, which provides a good prerequisite for efficient iodine capture on PTF. After loading silver nanoparticles onto PTF, as shown in the pore size distribution diagram in Fig. S2. The silver nanoparticles block a large number of microporous above 10 nm in PTF, which results in a decrease in the specific surface area of the material (1.935 m^2/g). However, this does not affect the hollow microtubule of the poplar fiber, and iodine vapor can still be efficiently captured by the active sites on the inner and outer interfaces. After iodine vapor capture, the specific surface area of the PTF@Ag^0NP decreases further (0.884 m^2/g), which is due to AgI caused by the chemical reaction of iodine vapor with silver nanoparticles to form a granular structure during the capture process [37]. Moreover, PTF@Ag^0NP shows almost consistent nitrogen adsorption and desorption curves before and after iodine vapor capture, indicating that the Ag nanoparticles and AgI produced do not damage the pore structure of PTF@Ag^0NP and have excellent stability.

XRD analysis

Figure 2c demonstrates the XRD diffraction patterns of PTF@Ag^0NP before and after iodine vapor capture. PTF@Ag^0NP shows distinct diffraction peaks of cellulose crystal structure at 2θ=15.8° and 22.5° [44], and exhibits diffraction peaks at 2θ = 38.2°,44.5°, 64.8°, and 77.5°, corresponding to the (111), (200), (220), and (311) crystal planes, respectively, displaying characteristic diffraction peaks of zero-valent silver (PDF: #04-0783) [45]. This indicates that Ag^+ is effectively reduced to Ag^0 after complexation with hydroxide and subsequent treatment

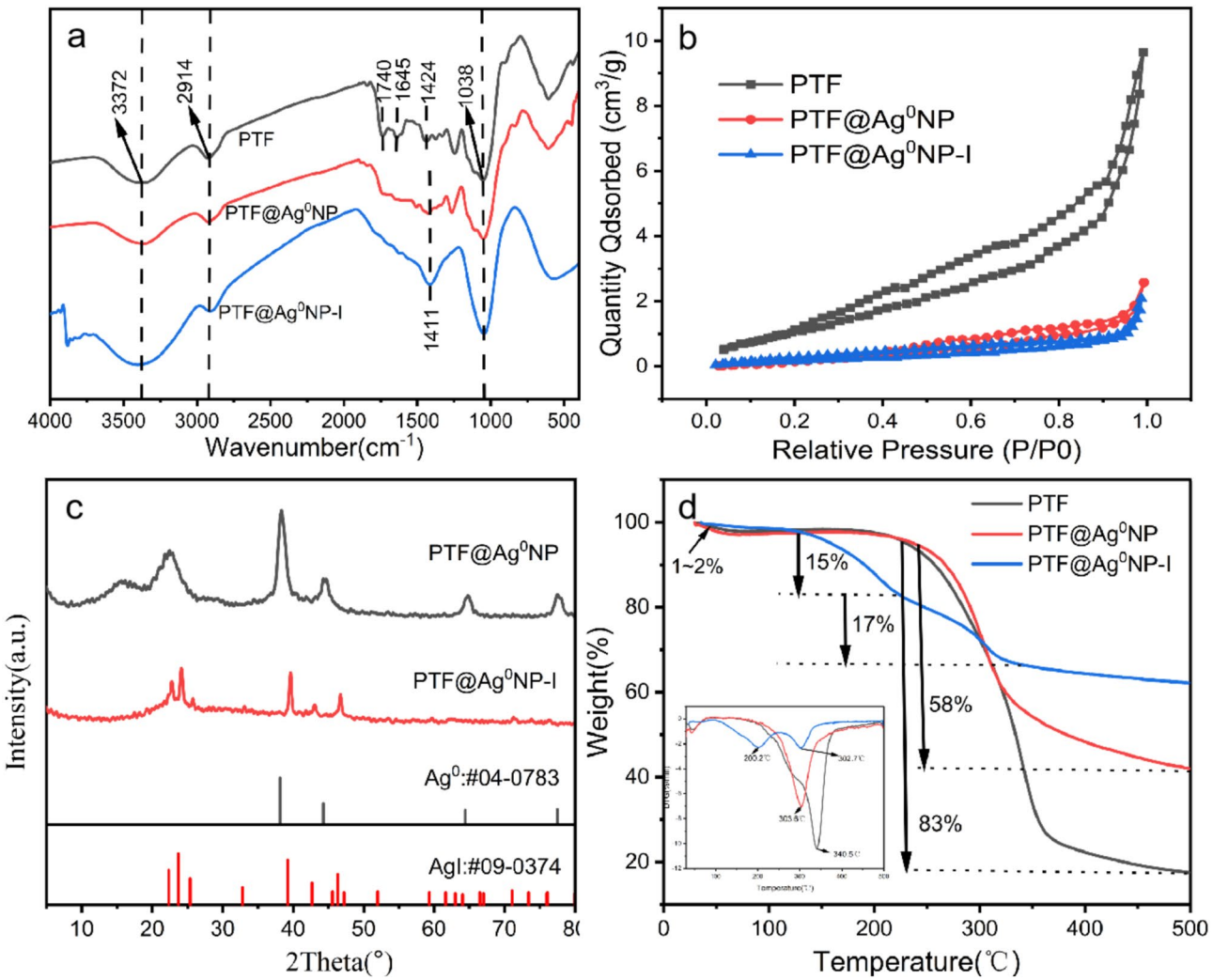

Fig. 2 (Color online) (**a**) FTIR spectra, (**b**) BET isotherms, (**c**) XRD patterns, and (**d**) TGA curves of PTF, PTF@Ag^0NP, and PTF@Ag^0NP-I

with sodium borohydride. After iodine capture, the crystal structure of cellulose in PTF@Ag^0NP disappeared, possibly because of the charge transfer occurring between iodine and the hydroxyl group on the cellulose crystal during iodine capture process, thereby diminishing the crystallinity of cellulose. PTF@Ag^0NP-I displays diffraction peaks at $2\theta = 22.5°$, 23.9°, 25.8°, 39.6°, 42.8°, 46.7°, and 71.1°, corresponding to the (100), (002), (101), (110), (103), (112), and (300) crystal planes, respectively, showing characteristic diffraction peaks of silver iodide (PDF: #09-0374) [46]. This indicates that Ag^0 and I_2 react chemically to form stable AgI, which effectively captures and immobilizes the iodine vapor.

TGA analysis

As shown in Fig. 2d, the TGA and DTG curve data before and after capturing the iodine vapor are recorded using the thermogravimetric analysis (TGA) method. PTF exhibits two different stages of mass loss. Before 60 °C, there is a 2 % mass loss, which is primarily attributed to the loss of moisture in the sample. Mass loss starts rapidly at 220 °C and reaches its maximum rate at 340.5 °C with a total mass loss of 82.3 %. The main reason for this stage of weight loss is the self-decomposition of the material [36]. The thermal stability trend of PTF@Ag^0NP is similar to PTF, but its mass loss at 500 °C is only 58 %, demonstrating higher heat resistance. After capturing the iodine vapor, PTF@Ag^0NP-I exhibits three different stages of mass loss. The mass loss before 60 °C is attributed to the residual moisture in the sample. Between 120 °C and 200 °C, a new stage of mass loss occurs, and the reference suggests that this mass loss is due to the evaporation and escape of iodine induced by the hydroxyl and carbonyl active sites on cellulose at high temperatures [43]. Finally, the mass loss near 302.7 °C is attributed to the self-decomposition of the material. Because 500 °C is below the decomposition temperature of silver

iodide at 558 °C [47], the mass loss of PTF@Ag^0NP-I at 500 °C is significantly lower than that of PTF@Ag^0NP. This indicates that iodine is primarily captured in the form of silver iodide, ultimately achieving the high-temperature immobilization of iodine vapor [40].

Morphology analysis

PTF, PTF@Ag^0NP, and PTF@Ag^0NP-I digital photos are shown in Figs. 3(a, c, e), respectively. PTF is a white fluffy fiber that turns brown after loading Ag^0NP and further exhibits a purple-brown color after capturing iodine vapor. In addition to the color change, the material maintains a fibrous structure without obvious morphological alterations, indicating that the loading of Ag^+ and the reduction process do not disrupt the structure of PTF. To study the microstructural changes of the materials during preparation as well as iodine capture, FE-SEM, EDS, and mapping characterization of the materials are shown in Fig. 3. The PTF fiber has a diameter of approximately 12 µm, and the surface and inner interface of the fiber channels are relatively smooth (Fig. 3a, b). After loading with nanosilver, PTF@Ag^0NP exhibits numerous nanoparticle-like substances on the surface (Fig. 3c, d), with particle diameters ranging from 30 µm to 100 µm (Fig. S3). It is speculated that these are silver nanoparticles loaded onto PTF. After iodine capture, the size of the nanoparticles increases significantly (Fig. 3e, f), and the particle diameter increases to between 50 µm and 350 µm (Fig. S3), which may be attributed to the successful capture and immobilization of iodine by the PTF@Ag^0NP, which converts the silver nanoparticles into AgI particles with larger particle sizes [27]. This is consistent with the XRD characterization results, which show that zero-valent silver reacts with iodine to form AgI [42]. The elemental mapping of PTF@Ag^0NP-I (Fig. 3h–k) shows that silver and iodine are uniformly distributed on PTF and their locations correspond closely to the positions of the nanosilver particles on PTF@Ag^0NP. This signifies the significant role played by the silver nanoparticles in PTF@Ag^0NP during the iodine vapor capture process.

3.3 Iodine vapor capture experiment

To evaluate the capture performance of PTF@Ag^0NP for iodine vapor, a 20 mg sample was placed in a vacuum at 75 °C for 24 h. Afterward, an iodine vapor capture experiment was conducted. The dynamic adsorption curve of PTF@Ag^0NP for iodine vapor was obtained by measuring the capture capacity of the material at different time intervals. As shown in Fig. 4a, the material exhibits a high capture efficiency for iodine vapor, and the capture amount gradually increases with increasing contact time. The dynamic adsorption equilibrium is reached after approximately 4 h, at which time the maximum iodine vapor capture is 1008.1 mg/g.

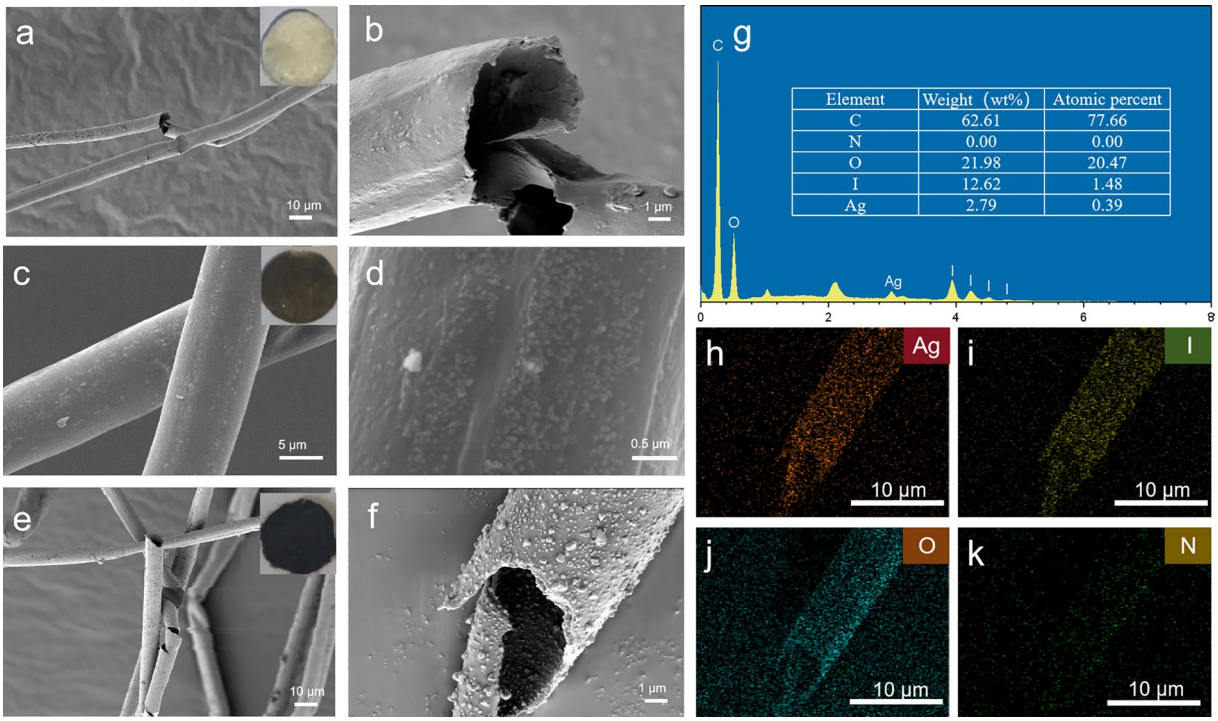

Fig. 3 (Color online) FE-SEM images of (**a**, **b**) PTF, (c, d) PTF@Ag^0NP, and (**e**, **f**) PTF@Ag^0NP-I (Pictures are corresponding digital photographs). Mapping images of (**g**) PTF@Ag^0NP-I and EDS images of (**h**) Ag, (**i**) I, (**j**) O, and (**k**) N, respectively

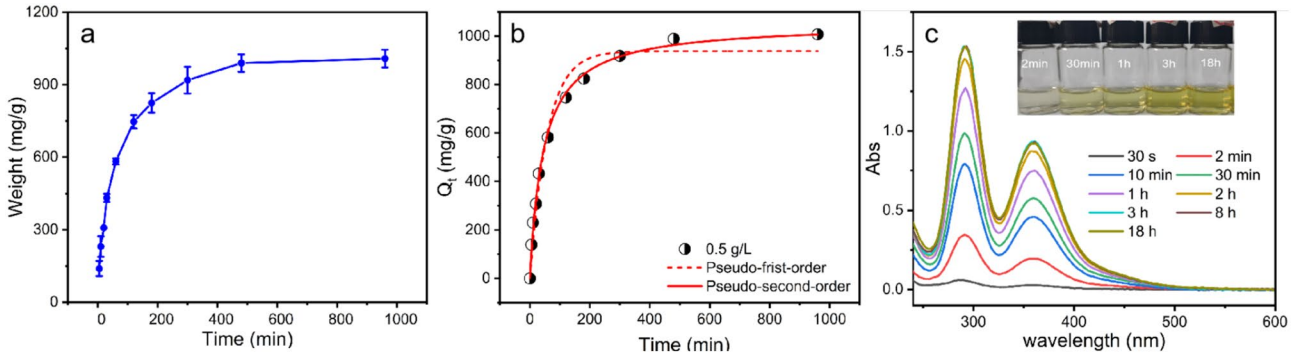

Fig. 4 (Color online) (**a**) change of the capture amount of iodine vapor with time, (**b**) adsorption kinetics fitting results of PCF@Ag^0NP, and (**c**) UV-Vis absorption spectra of iodine desorption in ethanol at different times

Table 1 Comparison of the capture capacity of different adsorbents for iodine vapor

Adsorbent	Temperature (°C)	Capture capacity (mg/g)	References
AgZ	–	135	[25]
Ag-Ni foam	200	456	[31]
Ag-HTX	150	429	[48]
NiTi-LDH	75	527	[40]
COF@CF	75	533.8	[49]
Ag@Mon-POF	70	250	[50]
Bi-Bi_2O_3-TiO_2-C	200	504	[51]
Cu-BTC	75	639	[52]
Ag-ETS-10	75	255	[53]
MXene-PIL	75	170	[54]
HT-Bi-ESCNF	200	1019	[43]
Ag^0@C/SiO_2	150	788	[55]
AgNPs@UiO-66	–	1260	[26]
NH-COF	80	2660	[56]
PTF@Ag^0NP	75	1008.1	This work

The adsorption curves are fitted using pseudo-first-order and pseudo-second-order kinetic equations. The results are presented in Fig. 4(b) and Table S3. The second-order kinetic model is more consistent with the iodine adsorption kinetics of PCF@Ag^0NP. The second-order kinetic correlation coefficient ($R^2 > 0.996$) is better than the first-order kinetic correlation coefficient ($R^2 > 0.974$), and the adsorption capacity calculated using the second-order kinetic calculation (Q_e = 1054.1 mg/g) is closer to the experimental value (Q_e = 1008.1 mg/g). This indicates that the adsorption process is not a simple physical adsorption dominated by diffusion, but a chemical reaction process dominated by rate control [31]. In addition, as shown in Fig. S4 and Table S3, the adsorption kinetics results of the materials prepared with 0.2 g/L and 2 g/L concentrations of silver nitrate are consistent with the above results, further verifying that iodine vapor capture by the material is dominated by chemisorption.

Table 1 compares the capture capacities of the PTF@Ag^0NP with those of the other adsorbents. MOF and COF materials, such as AgNPs@UiO-66 and NH-COF, exhibit stronger iodine vapor capture capabilities, but their production costs are high and their preparation processes are complicated, which makes them difficult to realize their industrial-scale applications. Many inorganic adsorbents such as NiTi-LDH, Bi-Bi_2O_3-TiO_2-C, and Cu-BTC have low capture capacities, which severely limits their development and use. Silver-based adsorbents like AgZ and Ag-HTX, which have lower capture capacities, have garnered extensive commercial applications owing to their strong capture stability. In comparison, PTF@Ag^0NP has a simple preparation process, a low preparation cost, and can be easily prepared on a large scale. Furthermore, the material demonstrates significantly higher iodine vapor capture than most silver-based adsorbents like AgZ, Ag-HTX, and Ag-ETS-10, while maintaining excellent capture stability. Considering these advantages, it is evident that the PTF@Ag^0NP is a potentially effective adsorbent for the removal of radioactive iodine vapor from spent fuel reprocessing exhaust gases.

To evaluate the iodine desorbed capability of PTF@Ag^0NP-I, the material was immersed in anhydrous ethanol at 25 °C for desorbed experiments. The iodine concentration in the desorption solution at different times was determined from the UV-Vis absorption spectra of the desorbed solutions. As shown in Fig. 4b, PTF@Ag^0NP-I exhibits excellent desorption efficiency, reaching desorbed equilibrium within 3 h. It is evident that the capture iodine in PTF@Ag^0NP-I is easily resolved, facilitating material regeneration and subsequent solidification treatment of radioactive iodine.

3.4 Iodine capture mechanism

TEM analysis

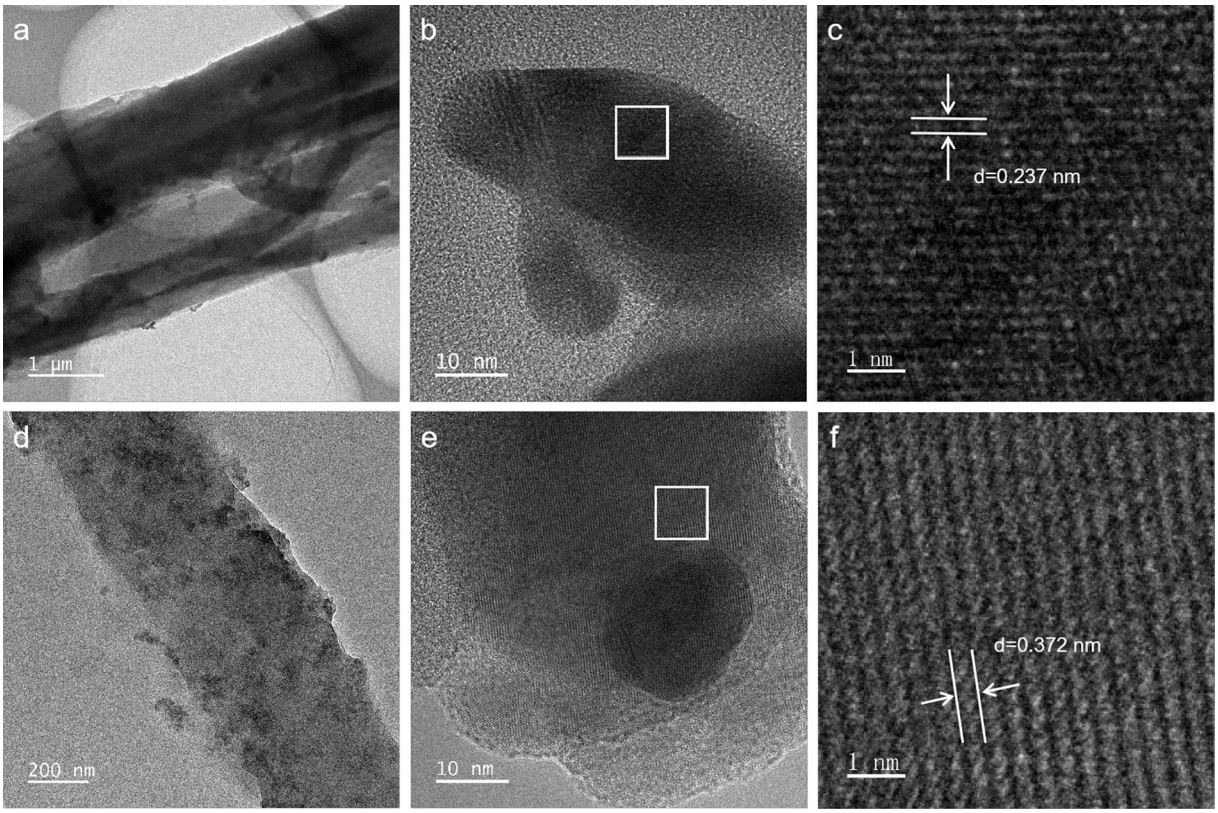

Fig. 5 (Color online) (**a**) TEM and (**b**, **c** HRTEM images of PTF@Ag^0NP. (**d**) TEM and (**e**, **f**) HRTEM images of PTF@Ag^0NP-I

To further explore the capture mechanism of PTF@Ag^0NP for iodine, the HRTEM characterization results before and after iodine capture by PTF@Ag^0NP are shown in Fig. 5. Before the iodine capture, numerous nanoscale particles were densely distributed at the interfaces and fiber pores of PTF (Fig. 5a, b). HRTEM reveals a crystal plane spacing of 0.237 μm, corresponding to the (111) crystal plane of zero-valent silver, further demonstrating the successful coordination of nanoscale zero-valent silver particles (Fig. 5c) [57]. After the iodine capture, the nanoscale particles are more dispersed at the material interface and pores (Fig. 5d, e). The HRTEM indicates a crystal plane spacing of 0.372 μm, corresponding to the (002) crystal plane of AgI (Fig. 5f) [58]. Consistent with the FE-SEM results (Fig. 3), it is further confirmed that during the iodine vapor capture process, zero-valent silver is confirmed to chemically react with iodine to form AgI to realize the capture and immobilization of iodine vapor.

XPS analysis

To further reveal the effect of the material on the capture of iodine vapor, the XPS technique was utilized to record the changes in the elemental valence states on the surface of the material (Fig. 6). Clear characteristic peaks of Ag 3*d* and I 3*d* appear in PTF@Ag^0NP-I (Fig. 6a), indicating that the material successfully coordinates silver and captures iodine. After capturing the iodine vapor, the Ag 3*d* characteristic peak positions shift from 374.3 eV and 368.3 eV to 374.0 eV and 368.0 eV, respectively (Fig. 6b, c), which demonstrates the transformation of Ag from Ag^0 to Ag^+ [55]. This indicates that silver plays an important role in the iodine capture process and its chemical reaction with iodine vapor. The O 1*s* characteristic peaks shift from 533.2 eV and 532.0 eV to 532.8 eV and 531.6 eV, respectively (Fig. 6e, f), which can be attributed to the induced adsorption of hydroxyl groups on iodine [27]. Finally, the I 3*d* characterization peaks at 630.4 eV and 618.9 eV indicate that iodine is mainly present as I^- in PTF@Ag^0NP-I (Fig. 6d), suggesting that the iodine in the material is stabilized and captured as a compound [43]. In addition, in the NIST database, AgI has the peaks at Ag $3d_{5/2} = 368.0 \pm 0.1$eV and I $3d_{5/2} = 619.0 \pm 0.2$eV [59], which is consistent with our experimental results (Ag $3d_{5/2} = 368.0$eV and I $3d_{5/2} = 618.9$eV). The characterization results provide strong evidence for the chemical reaction of zero-valent silver nanoparticles with iodine vapor to form AgI .

DFT analysis

To further understand the chelation stability of silver within PTF and the interaction mechanisms between PTF@

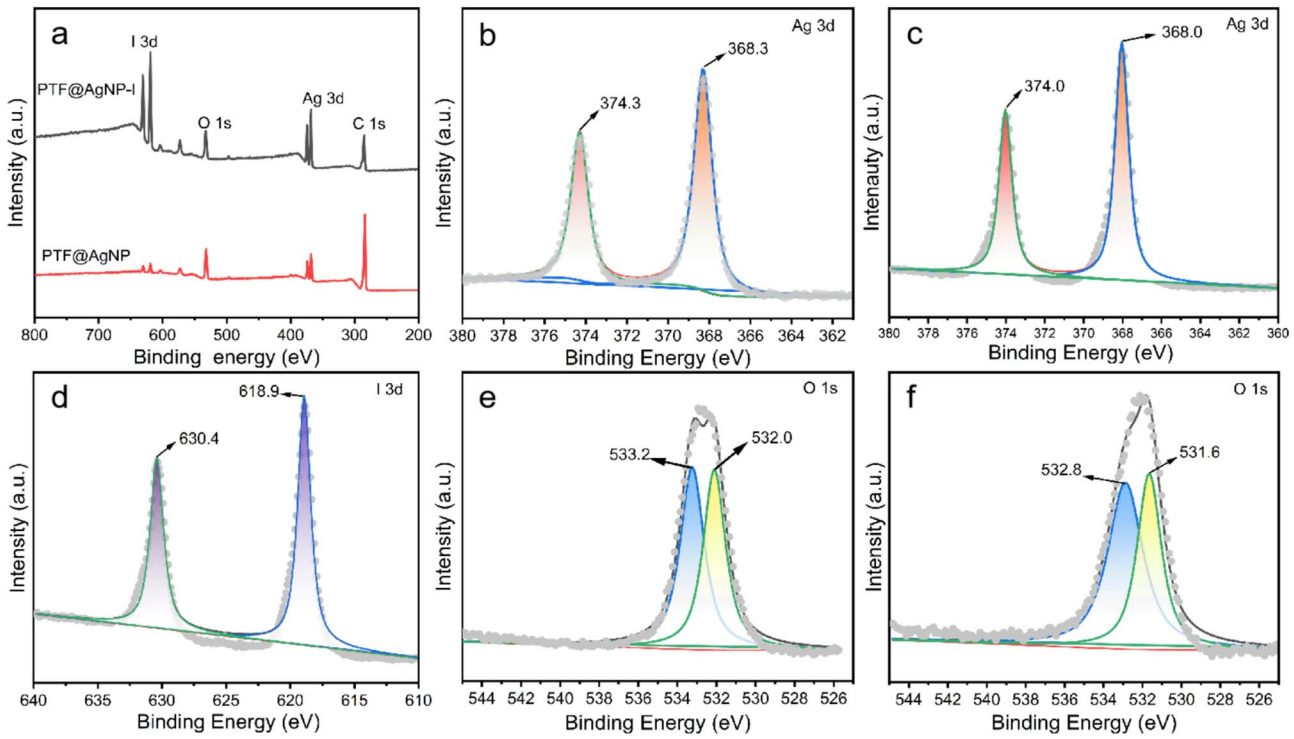

Fig. 6 (Color online) (**a**) XPS full spectra of PTF@Ag^0NP and PTF@Ag^0NP-I, deconvoluted element peak spectra of (**b**, **c**) Ag, (**d**) I, and (**e**, **f**) O

Ag^0NP and iodine vapor, cellulose chains, which constitute the basic structure of PTF, were investigated as substrates. The interactions between PTF, PTF@Ag^0NPs, and iodine molecules were analyzed in depth using density functional theory (DFT). As shown in Fig. 7a, the cellulose chains are linked together by β-type 1-4 glycosidic bonds consisting of D-pyranose glucose units (1–5 ring). To determine the optimal binding site for silver, 26 potential binding sites for silver were considered, including interstitial spaces, atomic top sites, and bridge sites between chemical bonds (Fig. S5A), and their binding energies were calculated separately. The results of the structural optimization (Fig. 7b) reveal that the site with the highest binding energy is T5 (located at the hydroxyl group at the top of the cellulose chain), with a binding energy of −0.46 eV. This indicates that silver can complex with the hydroxyl groups in cellulose through ion-dipole interactions, which agrees with the results of Capron et al. [28]. Subsequently, using T5 as the silver-binding site, a 5 ps ab initio molecular dynamics (AIMD) simulation was conducted within the NVT ensemble at 77 °C. Fig. 7c show that PTF@Ag^0NP has excellent stability with no displacement of the atomic sites, indicating that Ag^0NP can be stably loaded onto PTF.

Similarly, considering the potential 15 binding sites for I_2 molecules, the interaction between I_2 and PTF@Ag^0NP was computed, and the binding energies of the iodine molecules with PTF@Ag^0NP (Fig. S5B). Fig. 7d reveal that after structural optimization, all the iodine molecules are displaced to the S4 site and undergo a chemical reaction with Ag^0 to form AgI with a binding energy of −2.88 eV. During the reaction, the I-I bond breaks, generating new Ag-I bonds with lengths of 2.70 Å. This further confirms that PTF@Ag^0NP captured iodine through a chemical reaction between Ag^0 and I_2 to form AgI. The differential charge and Mulliken charge transfer for the binding of silver to PTF and the iodine capture by PTF@Ag^0NP were also studied. As shown in Fig. S6A, although only 0.06 eV of charge was transferred during the binding process of silver with PTF, the differential charge plot displayed a significant electron-donating trend with a large blue cloud between PTF and silver. Based on the binding energies and molecular dynamics calculations shown in Figs. 7c,d, it can be inferred that Ag is firmly complexed at the PTF interface. Fig. S6B illustrates the charge difference and Mulliken charge transfer after iodine capture by PTF@Ag^0NP, where iodine gains 0.25 eV of charge, whereas PTF@Ag^0NP loses 0.33 eV of charge. This signifies a strong chemical interaction between the iodine molecules and PTF@Ag^0NP, ultimately resulting in the effective capture of iodine.

As shown in Fig. 8, the iodine capture properties of the PTF@Ag^0NP are further discussed. The capture mechanism is divided into two parts. The first part is due to the soft

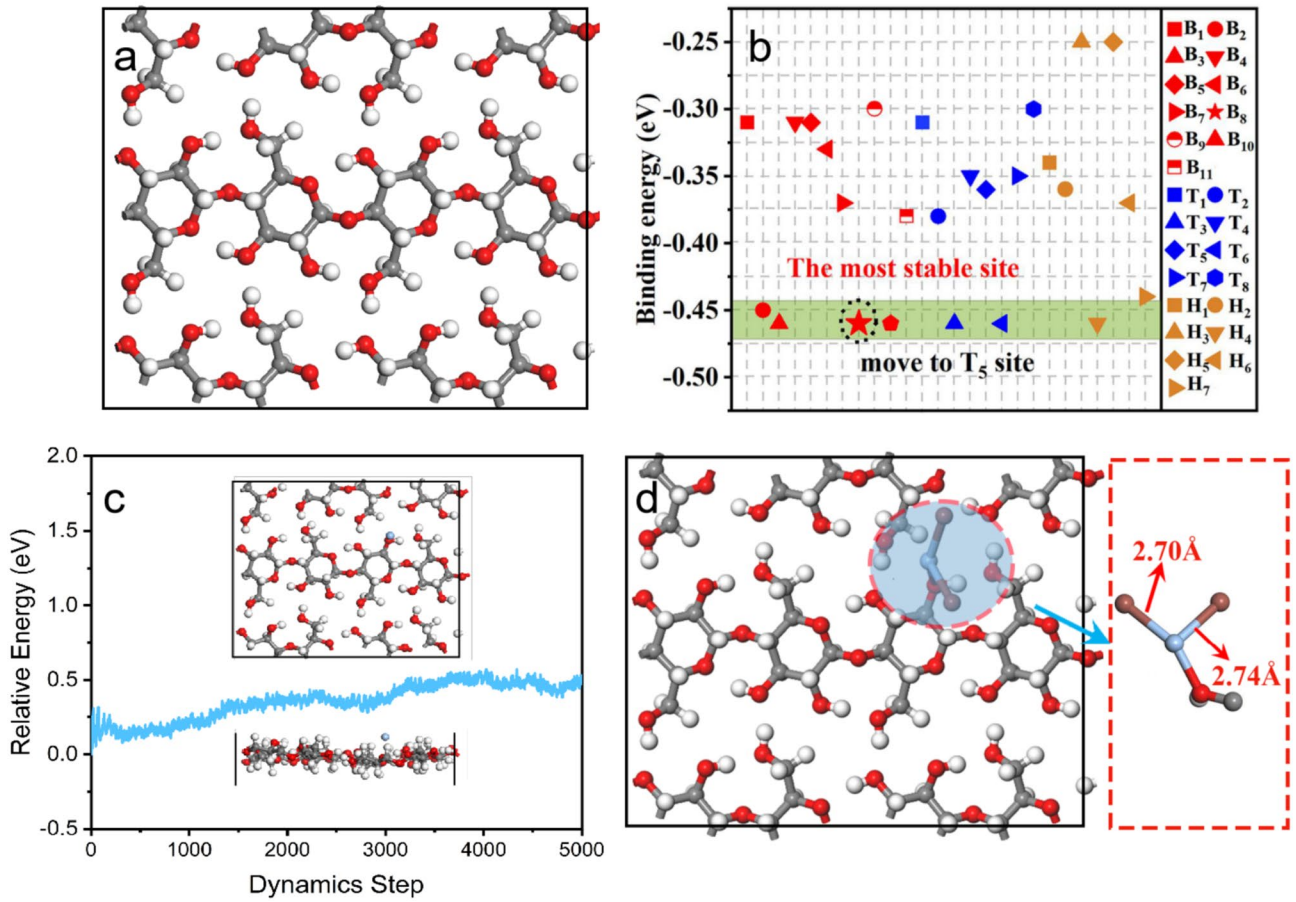

Fig. 7 (Color online) (**a**) Top view of the relaxed PTF, the gray, white, and red balls represent the C, H, and O atoms, respectively, (**b**) binding energies of Ag at various coordination sites on PTF, (**c**) molecular dynamics simulation of PTF@Ag^0NP, and (**d**) morphology of I_2 capture on PTF@Ag^0NP and corresponding bond lengths

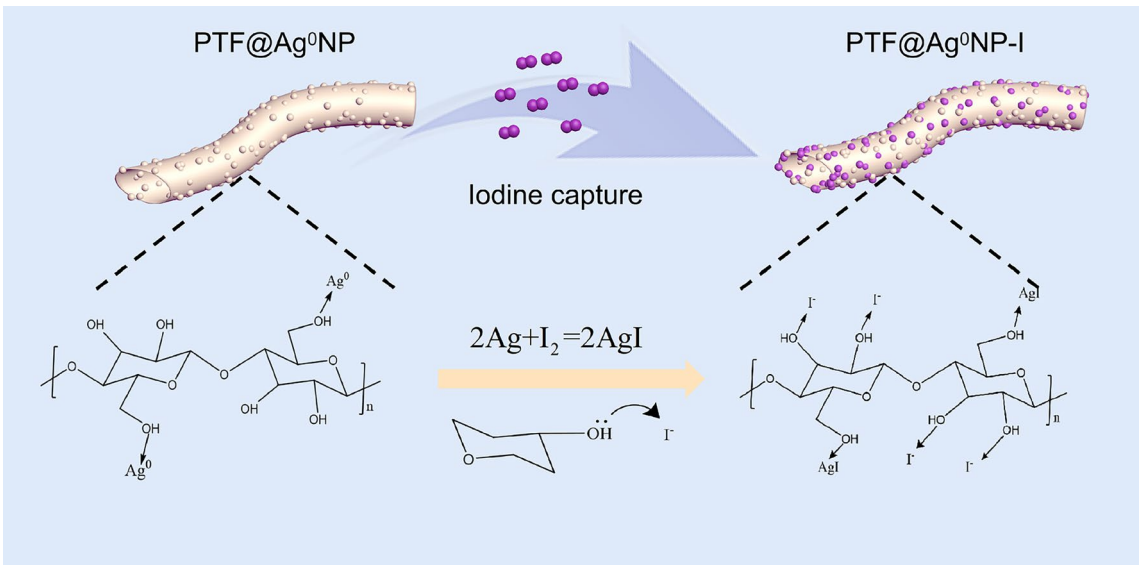

Fig. 8 (Color online) Schematic diagram of the mechanism for iodine vapor capture by PTF@Ag^0NP

Lewis acidic nature of the iodine molecules, with hydroxyl groups in the PTF having a strong adsorption–induction effect. During the contact of hydroxyl groups with iodine molecules, the ione electrons of the hydroxyl groups are transferred to the iodine molecules, resulting in polarization of the iodine molecules and their adsorption in the form of iodine anions induced by the hydroxyl groups [27]. The second part involves a chemical reaction between nanoscale zero-valent silver particles and iodine molecules to form a stable AgI compound at the PTF interface. This process results in the stabilization and immobilization of iodine vapor in PTF@Ag^0NP-I [55]. Meanwhile, after silver nanoparticles react to form silver iodide, silver iodide can further promote the aggregation of iodide ions around it [60] and enhance the induction capture ability of active groups such as hydroxyl in the PTF. In other words, zero-valent silver nanoparticles and active sites, such as hydroxyl groups, have a synergistic capture effect. In addition, because of the unique tubular structure of PTF, it significantly enhances contact between the active sites on cellulose and iodine. It also promotes the free shuttling of iodine vapor inside and outside the microtubules, resulting in a material with high capture efficiency and high iodine capture capacity.

4 Conclusion

In this study, a biomass-based composite functional material (PTF@Ag^0NP) was successfully synthesized by ultrasonic hydrothermal carbonization, which has a high iodine vapor capture capacity. The morphological structure and physicochemical properties of the material were revealed using FTIR, BET, XRD, TGA, and FE-SEM. The results indicate that the PTF@Ag^0NP exhibits rapid kinetics in capturing iodine vapor, with a maximum capture capacity of 1008.1 mg/g, showing significant advantages over similar silver-based capture materials. DFT calculations show that Ag^+ forms a strong complex with the hydroxyl groups in the PTF, Ag^0 has a high chemical reactivity toward iodine with an adsorption energy of −2.88 eV, and the iodine is finally captured in the form of silver iodide. HRTEM and XPS were used to reveal the capture mechanism. These findings reveal that iodine vapor is primarily captured through its reaction with Ag^0NP to form silver iodide. Additionally, the hydroxyl groups on the cellulose chains exhibit an inducing adsorption effect on the iodine molecules. The excellent iodine capture performance of PTF@Ag^0NP suggests that it has the potential to be a candidate capture material for the efficient removal of radioactive iodine from exhaust gases during spent fuel reprocessing.

Supplementary Information The online version contains supplementary material available at https://doi.org/10.1007/s41365-025-01647-x.

Author contributions All authors contributed to the study conception and design. Material preparation, data collection, and analysis were performed by Yu Fang, Pei Chen, and Fang Liu. Formal analysis, methodology, and writing–review and editing were performed by Hui Zhu, Yong Yi, and Jian Zhou. Supervision and conceptualization were performed by Tao Duan. Project administration, supervision, writing–review and editing were performed by Jie-Hong Lei. The first draft of the manuscript was written by Yu Fang and all authors commented on previous versions of the manuscript. All authors read and approved the final manuscript.

Data availability The data that support the findings of this study are openly available in Science Data Bank at https://cstr.cn/31253.11.sciencedb.j00186.00378 and https://www.doi.org/10.57760/sciencedb.j00186.00378.

Declarations

Conflict of interest The authors declare that they have no conflict of interest.

References

1. S.U. Nandanwar, K. Coldsnow, V. Utgikar et al., Capture of harmful radioactive contaminants from off-gas stream using porous solid sorbents for clean environment: A review. Chem. Eng. J. **306**, 369–381 (2016). https://doi.org/10.1016/j.cej.2016.07.073
2. J. Huve, A. Ryzhikov, H. Nouali et al., Porous sorbents for the capture of radioactive iodine compounds: a review. RSC Adv. **8**, 29248–29273 (2018). https://doi.org/10.1039/C8RA04775H
3. J. Ahad, M. Ahmad, A. Farooq et al., Removal of iodine by dry adsorbents in filtered containment venting system after 10 years of fukushima accident. Environ. Sci. Pollut. Res. **30**, 74628–74670 (2023). https://doi.org/10.1007/s11356-023-27485-1
4. P. Chen, H. Zhu, T. Na et al., Functionalized collagen fiber with specific recognition sites for highly efficient iodine capture: theoretical calculations and experimental verification. Chem. Eng. J. **476**, 146660 (2023). https://doi.org/10.1016/j.cej.2023.146660
5. C. Tan, Z. Xu, L. Zhang et al., Introducing zirconium organic gels for efficient radioiodine gas removal. Inorg. Chem. **61**, 4818–4824 (2022). https://doi.org/10.1021/acs.inorgchem.1c03159
6. B.J. Riley, J.D. Vienna, D.M. Strachan et al., Materials and processes for the effective capture and immobilization of radioiodine: A review. J. Nucl. Mater. **470**, 307–326 (2016). https://doi.org/10.1016/j.jnucmat.2015.11.038
7. H. Zhu, B. Wang, W. Zhu et al., Space and structure activation of collagen fiber for high efficient capture iodine in off-gas. Colloids Surf. Physicochem. Eng. Asp. **617**, 126389 (2021). https://doi.org/10.1016/j.colsurfa.2021.126389
8. C. Chien, Y. Huang, W. Wang et al., Efficiency of moso bamboo charcoal and activated carbon for adsorbing radioactive iodine. Clean: Soil, Air, Water **39**, 103–108 (2011). https://doi.org/10.1002/clen.201000012
9. J. Zhou, Q. Chen, T. Li et al., Porous copper-loaded zeolites for high-efficiency capture of iodine from spent fuel reprocessing off-gas. Inorg. Chem. **61**, 7746–7753 (2022). https://doi.org/10.1021/acs.inorgchem.1c03986
10. B.J. Riley, J.O. Kroll, J.A. Peterson et al., Silver-loaded aluminosilicate aerogels as iodine sorbents. ACS Appl. Mater. Interfaces. **9**, 32907–32919 (2017). https://doi.org/10.1021/acsami.7b10290
11. Y. Zhang, L. He, T. Pan et al., Superior iodine uptake capacities enabled by an open metal-sulfide framework composed of three

types of active sites. Chin. Chem. Soc. **57**, 1540–1548 (2022). https://doi.org/10.31635/ccschem.022.202201966
12. X. Liu, A. Zhang, R. Ma et al., Experimental and theoretical insights into copper phthalocyanine-based covalent organic frameworks for highly efficient radioactive iodine capture. Chin. Chem. Lett. **33**, 3549–3555 (2022). https://doi.org/10.1016/j.cclet.2022.03.001
13. K.W. Chapman, P.J. Chupas, T.M. Nenoff, Radioactive iodine capture in silver-containing mordenites through nanoscale silver iodide formation. J. Am. Chem. Soc. **132**, 8897–8899 (2010). https://doi.org/10.1021/ja103110y
14. J. Zhou, T. Lan, T. Li et al., Highly efficient capture of iodine in spent fuel reprocessing off-gas by novelly porous copper-doped silica zeolites. Sep. Purif. Technol. **290**, 120895 (2022). https://doi.org/10.1016/j.seppur.2022.120895
15. H. Liu, X. Zhang, Z. Lv et al., Ternary heterostructure membranes with two-dimensional tunable channels for highly selective ion separation. JACS. Au. **3**, 3089–3100 (2023). https://doi.org/10.1021/jacsau.3c00473
16. J. Liang, T. Liu, Y. Li et al., 2D vertical heterostructure membranes for lanthanide separation. Cell Rep. Phys. Sci. **3**, 100769 (2022). https://doi.org/10.1016/j.xcrp.2022.100769
17. J.Y. Yang, X. Chang, F. Wei et al., High performance photocatalyst TiO_2@UiO-66 applied to degradation of methyl orange. Discover Nano. **18**, 2731–9229 (2023). https://doi.org/10.1186/s11671-023-03894-6
18. X. Chang, P.Z. Hu, H.L. Liu et al., ZIF-8 modified graphene oxide/sodium alginate 3D elastic spheres for uranium trapping in seawater. Desalination **549**, 116371 (2023). https://doi.org/10.1016/j.desal.2023.116371
19. E.D. Miensah, M.M. Khan, J.Y. Chen et al., Zeolitic imidazolate frameworks and their derived materials for sequestration of radionuclides in the environment: A review. Crit. Rev. Env. Sci. Tech. **50**, 1874–1934 (2020). https://doi.org/10.1080/10643389.2019.1686946
20. P. Wang, B.B. Qi, A.T. Gu et al., An economical modification method for MIL-101 to capture radioiodine gaseous: adsorption properties and enhancement mechanism. Adsorpt. Sci. Technol. **11**, 4126562 (2023). https://doi.org/10.1155/2023/4126562
21. X.H. Liang, G.Y. Chen, H. Zhang et al., Co-adsorption performance of iodine and NO_X in iodine exhaust gas by NH_2-MIL-125. J. Hazard. Mater. **470**, 134237 (2024). https://doi.org/10.1016/j.jhazmat.2024.134237
22. D.F. Sava, K.W. Chapman, M.A. Rodriguez et al., Competitive I2 sorption by Cu-BTC from humid gas streams. Chem. Mater. **25**, 2591–2596 (2013). https://doi.org/10.1021/cm401762g
23. Z.J. Tian, T.S. Thee, Y.X. Hao et al., Hollow Bismuth-based nanoreactor with ultrathin disordered mesoporous silica shell for superior radioactive iodine decontamination. Chem. Bio. Eng. **6**, 548–558 (2024). https://doi.org/10.1021/cbe.4c00010
24. C. Muhire, A. Tesfay Reda, D. Zhang et al., An overview on metal oxide-based materials for iodine capture and storage. Chem. Eng. J. **431**, 133816 (2022). https://doi.org/10.1016/j.cej.2021.133816
25. A.I. Wiechert, A.P. Ladshaw, J. Moon et al., Capture of iodine from nuclear-fuel-reprocessing off-gas: influence of aging on a reduced silver mordenite adsorbent after exposure to NO/NO_2. ACS Appl. Mater. Interfaces. **12**, 49680–49693 (2020). https://doi.org/10.1021/acsami.0c15456
26. Y. Feng, P. Yang, Y. Li et al., AgNPs-containing metal-organic frameworks for the effective adsorption and immobilization of radioactive iodine. J. Chem. Eng. Data **65**, 1986–1992 (2020). https://doi.org/10.1021/acs.jced.9b01146
27. B. Wang, H. Zhu, T. Duan et al., Multi-layer active interface construction with polyphenols and nano-silver on nano collagen fiber for efficient capturing iodine vapor. Appl. Surf. Sci. **596**, 153585 (2022). https://doi.org/10.1016/j.apsusc.2022.153585
28. D. Musino, C. Rivard, G. Landrot et al., Hydroxyl groups on cellulose nanocrystal surfaces form nucleation points for silver nanoparticles of varying shapes and sizes. J. Colloid Interface Sci. **584**, 360–371 (2021). https://doi.org/10.1016/j.jcis.2020.09.082
29. M. Li, Y. Li, Q. An et al., Green planting silver nanoparticles on Populus fibers and the catalytic application. Res. Chem. Intermed. **44**, 5669–5681 (2018). https://doi.org/10.1007/s11164-018-3447-4
30. L.H. Fu, B. Liu, L.Y. Meng et al., Comparative study of cellulose/Ag nanocomposites using four cellulose types. Mater. Lett. **171**, 277–280 (2016). https://doi.org/10.1016/j.matlet.2016.02.118
31. Z. Tian, T.S. Chee, L. Zhu et al., Comprehensive comparison of bismuth and silver functionalized nickel foam composites in capturing radioactive gaseous iodine. J. Hazard. Mater. **417**, 125978 (2021). https://doi.org/10.1016/j.jhazmat.2021.125978
32. B. Delley, An all-electron numerical method for solving the local density functional for polyatomic molecules. J. Chem. Phys. **92**, 508–517 (1990). https://doi.org/10.1063/1.458452
33. J.P. Perdew, K. Burke, M. Ernzerhof, Generalized gradient approximation made simple. Phys. Rev. Lett. **77**, 3865–3868 (1996). https://doi.org/10.1103/PhysRevLett.77.3865
34. S. Grimme, Semiempirical GGA-type density functional constructed with a long-range dispersion correction. J. Comput. Chem. **27**, 1787–1799 (2006). https://doi.org/10.1002/jcc.20495
35. M. Likon, M. Remškar, V. Ducman et al., Populus seed fibers as a natural source for production of oil super absorbents. J. Environ. Manage. **114**, 158–167 (2013). https://doi.org/10.1016/j.jenvman.2012.03.047
36. M. Li, Y. Gong, A. Lyu et al., The applications of populus fiber in removal of Cr(VI) from aqueous solution. Appl. Surf. Sci. **383**, 133–141 (2016). https://doi.org/10.1016/j.apsusc.2016.04.167
37. H.E. Emam, M.K. El-Bisi, Merely Ag nanoparticles using different cellulose fibers as removable reductant. Cellulose **21**, 4219–4230 (2014). https://doi.org/10.1007/s10570-014-0438-5
38. P. Raveendran, J. Fu, S.L. Wallen, Completely Green synthesis and stabilization of metal nanoparticles. J. Am. Chem. Soc. **125**, 13940–13941 (2003). https://doi.org/10.1021/ja029267j
39. H. Zhou, J. Zhou, T. Wang et al., In-situ preparation of silver salts/collagen fiber hybrid composites and their photocatalytic and antibacterial activities. J. Hazard. Mater. **359**, 274–280 (2018). https://doi.org/10.1016/j.jhazmat.2018.07.043
40. G. Lin, L. Zhu, T. Duan et al., Efficient capture of iodine by a polysulfide-inserted inorganic NiTi-layered double hydroxides. Chem. Eng. J. **378**, 122181 (2019). https://doi.org/10.1016/j.cej.2019.122181
41. L. Li, R. Chen, Y. Li et al., Novel cotton fiber-covalent organic framework hybrid monolith for reversible capture of iodine. Cellulose **27**, 5879–5892 (2020). https://doi.org/10.1007/s10570-020-03189-4
42. K.V. Gensh, P.V. Kolosov, N.G. Bazarnova et al., Quantitative analysis of cellulose nitrates by fourier transform infrared spectroscopy. Russ. J. Bioorganic Chem. **37**, 814–816 (2011). https://doi.org/10.1134/S1068162011070077
43. Z. Tian, T.S. Chee, X. Zhang et al., Novel bismuth-based electrospinning materials for highly efficient capture of radioiodine. Chem. Eng. J. **412**, 128687 (2021). https://doi.org/10.1016/j.cej.2021.128687
44. L. Li, R. Chen, Y. Li, Novel cotton fiber-covalent organic framework hybrid monolith for reversible capture of iodine. Cellulose **07**, 5879–5892 (2022). https://doi.org/10.1007/s10570-020-03189-4
45. W. Huang, C. Jing, X. Zhang et al., Integration of plasmonic effect into spindle-shaped MIL-88A(Fe): steering charge flow for enhanced visible-light photocatalytic degradation of ibuprofen. Chem. Eng. J. **349**, 603–612 (2018). https://doi.org/10.1016/j.cej.2018.05.121

46. H. Yu, B. Huang, H. Wang et al., Facile construction of novel direct solid-state Z-scheme AgI/BiOBr photocatalysts for highly effective removal of ciprofloxacin under visible light exposure: Mineralization efficiency and mechanisms. J. Colloid Interface Sci. **522**, 82–94 (2018). https://doi.org/10.1016/j.jcis.2018.03.056
47. M. Reháková, A. Sopková, K. Jesenák et al., Thermal analysis of the synthetic zeolite ZSM5 and its silver iodide form. J. Therm. Anal. **50**, 505–509 (1997). https://doi.org/10.1007/BF01980510
48. S. Chong, B.J. Riley, W. Kuang et al., Iodine capture with mechanically robust heat-treated Ag-Al-Si-O xerogel sorbents. ACS Omega **6**, 11628–11638 (2021). https://doi.org/10.1021/acsomega.1c00852
49. Y. Li, Y. Li, Q. Zhao et al., Cotton fiber functionalized with 2D covalent organic frameworks for iodine capture. Cellulose **27**, 1517–1529 (2020). https://doi.org/10.1007/s10570-019-02877-0
50. A.P. Katsoulidis, J. He, M.G. Kanatzidis, Functional monolithic polymeric organic framework aerogel as reducing and hosting media for Ag nanoparticles and application in capturing of iodine vapors. Chem. Mater. **24**, 1937–1943 (2012). https://doi.org/10.1021/cm300696g
51. H. Zou, F. Yi, M. Song et al., Novel synthesis of Bi-Bi_2O_3-TiO_2-C composite for capturing iodine-129 in off-gas. J. Hazard. Mater. **365**, 81–87 (2019). https://doi.org/10.1016/j.jhazmat.2018.11.001
52. Q. Zhao, L. Zhu, G. Lin et al., Controllable synthesis of Porous Cu-BTC@polymer composite beads for iodine capture. ACS Appl. Mater. Interfaces. **11**, 42635–42645 (2019). https://doi.org/10.1021/acsami.9b15421
53. L. Wu, J.A. Sawada, D.B. Kuznicki et al., Iodine adsorption on silver-exchanged titania-derived adsorbents. J. Radioanal. Nucl. Chem. **302**, 527–532 (2014). https://doi.org/10.1007/s10967-014-3252-5
54. S. Sun, X. Sha, J. Liang et al., Rapid synthesis of polyimidazole functionalized MXene via microwave-irradiation assisted multi-component reaction and its iodine adsorption performance. J. Hazard. Mater. **420**, 126580 (2021). https://doi.org/10.1016/j.jhazmat.2021.126580
55. Y. Xiong, Y. Ai, H. Wang et al., High capacity adsorption of iodine gas by Ag^0@C/SiO_2 derived from rice husk: synergistic effect between C/SiO_2 supports and Ag^0 sites. J. Radioanal. Nucl. Chem. **332**, 3059–3068 (2023). https://doi.org/10.1007/s10967-023-08973-7
56. N. Mokhtari, M. Dinari, Developing novel amine-linked covalent organic frameworks towards reversible iodine capture. Sep. Purif. Technol. **301**, 121948 (2022). https://doi.org/10.1016/j.seppur.2022.121948
57. G. Hu, J. Cao, Occurrence and significance of natural ore-related Ag nanoparticles in groundwater systems. Chem. Geol. **515**, 9–21 (2019). https://doi.org/10.1016/j.chemgeo.2019.03.036
58. Q. Huang, S. Wen, X. Zhu et al., Synthesis and characterization of an AgI/Ag hybrid nanocomposite with surface-enhanced raman scattering performance and photocatalytic activity. RSC Adv. **4**, 37187–37192 (2014). https://doi.org/10.1039/C4RA04639K
59. V.K. Kaushik, XPS core level spectra and auger parameters for some silver compounds. J. Election. Spectrosc. **56**, 273–277 (1991). https://doi.org/10.1016/0368-2048(91)85008-h
60. W. Mu, Q. Yu, X. Li et al., Niobate nanofibers for simultaneous adsorptive removal of radioactive strontium and iodine from aqueous solution. J. Alloys Compd. **693**, 550–557 (2017). https://doi.org/10.1016/j.jallcom.2016.09.200